

PAPER • OPEN ACCESS

Plasmonic properties of aluminium nanowires in amorphous silicon






To cite this article: Annett Thøgersen *et al* 2023 *J. Phys.: Condens. Matter* **35** 065301

View the [article online](#) for updates and enhancements.

You may also like

- [Nanoscale mapping of shifts in dark plasmon modes in sub 10 nm aluminum nanoantennas](#)
Kenan Elibol, Clive Downing and Richard G Hobbs
- [Performance enhancement of ultraviolet light emitting diode incorporating Al nanohole arrays](#)
Jie'an Jiang, Wei Guo, Houqiang Xu et al.
- [Low-cost and simple fabrication of hierarchical Al nanopit arrays for deep ultraviolet refractive index sensing](#)
Huimin Wang, Liqing Huang, Yu Zhang et al.

Plasmonic properties of aluminium nanowires in amorphous silicon

Annett Thøgersen^{1,*} , Ingvild J T Jensen¹, Branson D Belle¹ , Marit Stange¹,
Vilde Mari Reinertsen² , Torunn Kjeldstad², Øystein Prytz² , Edouard Monakhov²
and Demie Kepaptsoglou^{3,4} 

¹ SINTEF Industry, PO Box 124 Blindern, 0314 Oslo, Norway

² Department of Physics, Centre for Materials Science and Nanotechnology, University of Oslo,
PO Box 1048 Blindern, N-0316 Oslo, Norway

³ SuperSTEM, SciTech Daresbury Science and Innovation Campus, Keckwick Lane, Daresbury WA4

4AD, United Kingdom

⁴ Department of Physics, University of York, Heslington YO10 5DD, United Kingdom

E-mail: annett.thogersen@sintef.no

Received 9 September 2022, revised 11 November 2022

Accepted for publication 15 November 2022

Published 14 December 2022



CrossMark

Abstract

Plasmonic structures can help enhance optical activity in the ultraviolet (UV) region and therefore enhancing photocatalytic reactions and the detection of organic and biological species. Most plasmonic structures are composed of Ag or Au. However, producing structures small enough for optical activity in the UV region has proved difficult. In this study, we demonstrate that aluminium nanowires are an excellent alternative. We investigated the plasmonic properties of the Al nanowires as well as the optoelectronic properties of the surrounding *a-Si* matrix by combining scanning transmission electron microscopy imaging, electron energy loss spectroscopy and electrodynamic modelling. We have found that the Al nanowires have distinct plasmonic modes in the UV and far UV region, from 0.75 eV to 13 eV. In addition, simulated results found that the size and spacing of the Al nanowires, as well as the embedding material were shown to have a large impact on the type of surface plasmon energies that can be generated in the material. Using electromagnetic modelling, we have identified the modes and illustrated how they could be tuned further.

Supplementary material for this article is available [online](#)

Keywords: nanowires, plasmon, TEM, EELS, modelling

(Some figures may appear in colour only in the online journal)

1. Introduction

Research into the plasmonic properties of metallic films and particles has intensified recently and is now focused

on a variety of applications such as energy harvesting [1, 2], enhanced light–matter interaction [3], highly sensitive detection of chemicals [4], catalysis [5], optoelectronics [6], nano-optics [7], nanoantennas [8], photocathodes [9], and enhancement of high energy photochemical reactions [10]. Plasmon enhancement of the photochemical reactions of gas phase molecules, such as CO, O₂, and H₂O, will require very high plasmon energies because of their electronic absorption bands in the vacuum ultraviolet region (VUV) that is below 200 nm (above 6.2 eV) [10, 11]. Exciting the necessary plasmons for use in these types of devices are challenging with

* Author to whom any correspondence should be addressed.



Original Content from this work may be used under the terms of the [Creative Commons Attribution 4.0 licence](#). Any further distribution of this work must maintain attribution to the author(s) and the title of the work, journal citation and DOI.

normal plasmonic metals, such as silver (Ag) and gold (Au) [10]. Conversely with aluminum (Al), it is possible to produce plasmon resonances that can extend into the UV region, shifting the plasmon wavelength from 570 nm (2.2 eV) to 270 nm (4.6 eV) by changing the particle diameter from 180 nm to 70 nm [8, 12–14]. This is because the d-bands of Al lie above the Fermi level, as well as Al having higher electron densities (three valence electrons per atom) and lower screening [8].

The plasmonic properties of silver or gold particles larger than 20 nm in vacuum have been investigated by electron energy loss spectroscopy (EELS) and transmission electron microscopy (TEM) [15–20]. However, smaller plasmonic nanoparticles can be more difficult to investigate in a TEM since the loss probability is proportional to the induced electric field which is inversely proportional to the size [21]. The embedding of the particle is also a challenge because of damping. When the plasmon energy is above the band gap of the embedding matrix, coupling between the surface plasmon (SP) and states in the matrix can occur, which induces energy transfer from the particle to the matrix. Such energy transfer can result in an observable broadening of the plasmon peaks in the EEL spectrum [22]. Fully embedded particles have been investigated with EELS before, however their plasmon energies were below the band gap of the matrix [23, 24]. In this paper, we present the plasmonic properties of Al nanowires (AINWs) embedded in an amorphous Si matrix ($a-Si$) by high resolution EELS using a scanning TEM (STEM) and modelling. In this system most of the SP peak energies are above the $a-Si$ band gap. Despite the low intensity and broad peaks, the combination of modelling and data analysis of TEM measurements allowed us to make significant progress in understanding the plasmonic properties of this promising system.

2. Methodology

Thin films of Al and Si were deposited on mono-crystalline Si (100) substrates by magnetron sputtering using a CVC 601. The system consisted of two 8'' targets with a normal sputter angle and a 6 cm distance between the substrate and targets. The deposition was performed at room temperature with thin alternating layers of approximately 40 at.% Al and 60 at.% Si. A power setting of 400 W for Si and 150 W for Al was used with a substrate rotation of 2.5 rpm and sputtering time of 22 min, resulting in an overall film thickness of 100 nm. More details on the synthesis, growth and analysis can be found in our previous work [25–28].

Standard cross-sectional TEM samples were prepared by ion-polishing with a PIPS ion polishing system from Gatan. Plane-view samples were prepared using an Allied High Tech—MultiPrep Polishing System with a wedge angle of 2°. The samples were analyzed using a Nion UltraSTEM-100MC ‘HERMES’, aberration corrected, monochromated dedicated STEM instrument, equipped with a Gatan Enfium RS spectrometer. The microscope was operated at 60kV, with an energy resolution of 15 meV, determined by the position of the energy width selection slit. Further analysis was performed

using a monochromated FEI Titan G2 60–300 microscope operated at 60 kV using high resolution STEM and EELS with a Gatan Quantum 965 EELS spectrometer. The simulations of SPs were performed using ANSYS Lumerical’s Finite Difference Time Domain (FDTD) software [29], and the metal nanoparticle boundary element method (MNPBEM) [30]. Details of the EELS analysis (figure S3) and simulations can be found in the supplementary information (SI).

3. Results and discussion

Figures 1(A) and (B) show bright field TEM images of the self-organizing AINWs in $a-Si$ in cross-sectional and plane-view, respectively. It can be observed that the AINWs extend throughout the 100 nm thick $a-Si$ layer. In figure 1(C) a fast Fourier transformed (FFT) image shows the diffraction patterns from the various AINWs in figure 1(A), while figure 1(D) shows the crystallinity of an AINW. The FFT image shows both the diffuse rings from the amorphous silicon matrix and the distinct diffraction spots from the crystalline AINWs, showing that the AINWs are crystalline with different orientations. From the plane-view image (figure 1(B)) we can see that the AINWs are approximately 3–5 nm in diameter, and are packed close together in a random network, with a distance of approximately 1.5–2.5 nm. More details on the structure and wire separation can be seen in the SI.

3.1. Initial numerical approximation

To rationalize the experimental results, numerical calculations of plasmon modes were performed. The AINWs were first simulated with a length of 50 nm and a diameter of 5 nm in vacuum. The experimental wires investigated had different lengths, depending on the view, that is around 20 nm in the cross-sectional view and around 70 nm in the plane-view. Therefore, we chose an intermediate length but we show in the SI how the different modes are influenced by a change in the length of the wire (see figures S4 and S5). We simulated SPs excited by both light (FDTD method) and an electron beam (MNPBEM). Figure 2(A) illustrates the two different polarization directions of the plane wave source and two different electron beam directions. The scanning path of the beam is also illustrated. The paths and directions were selected to represent the two views from the STEM measurements, plane, and cross-sectional. The average loss probability, \bar{P}_{loss} , spectra from the paths are used in the plotted spectra.

In figure 2(B), the absorption cross section, σ_{abs} , spectra from the light excitations showed one main peak for each polarization direction. First, the plasmon oscillates with longitudinal modes (red spectrum) when the external electric field is parallel to the wire length. There were two peaks around 1.5 eV. This could be a result of hybrid SP-interband modes since Al has a narrow interband spectral band at 1.5 eV [13]. The mode that is potentially hybridizing with the interband mode is the longitudinal dipole mode which has a resonance peak at 2.1 eV. Additional higher-order longitudinal modes were also observed at higher energies, with the strongest at 4.9 eV. Second, the plasmon oscillates in transverse modes

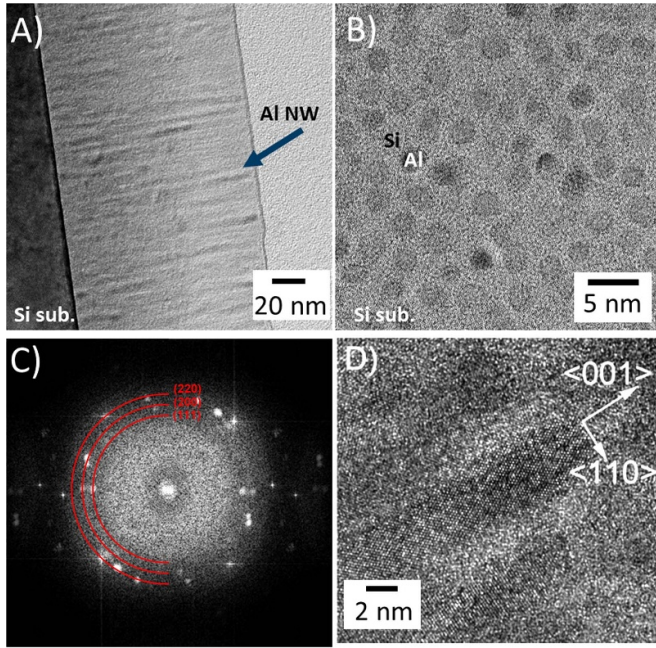


Figure 1. TEM images of (A) cross-section sample and (B) plane-view sample, (C) FFT diffractogram of (A), and (D) crystal structure of an AlNW where the directions are shown for the central NW.

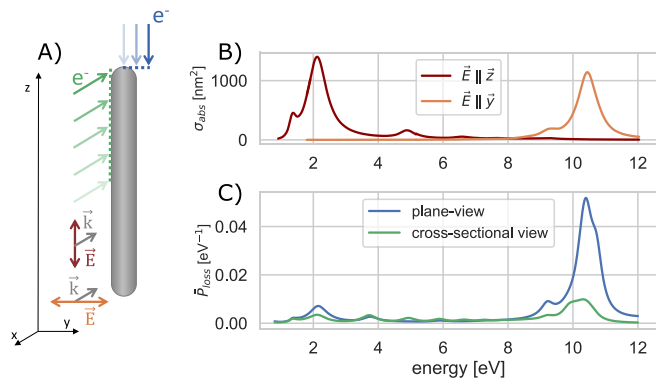


Figure 2. (A) Illustration of electron beam direction and path (green and blue) and plane wave polarization direction (red and orange). (B) Absorption cross section of NW for the two polarization directions illustrated in (A) and calculated with the FDTD method. (C) Simulated EELS spectra for the two different views (electron beam directions) shown in (A) and calculated with MNPBEM.

(orange spectrum) with an external electric field normal to the AlNW length. The dipole transverse mode had a resonance energy of 10.4 eV. This peak can also be seen in both views in figure 2(C), from the loss probability (\bar{P}_{loss}) spectra calculated using an electron beam source. However, it is not a single peak, but a convolution of two peaks. Both views have a peak at 10.4 eV, in the plane-view, there is an additional peak at 10.7 eV and in the cross-sectional view, there is an additional one at 10.0 eV. These peak energies were extracted by curve-fitting the simulated spectra with a sum of two Lorentzian functions. Additionally, the \bar{P}_{loss} in figure 2(C) shows several modes at lower energies including

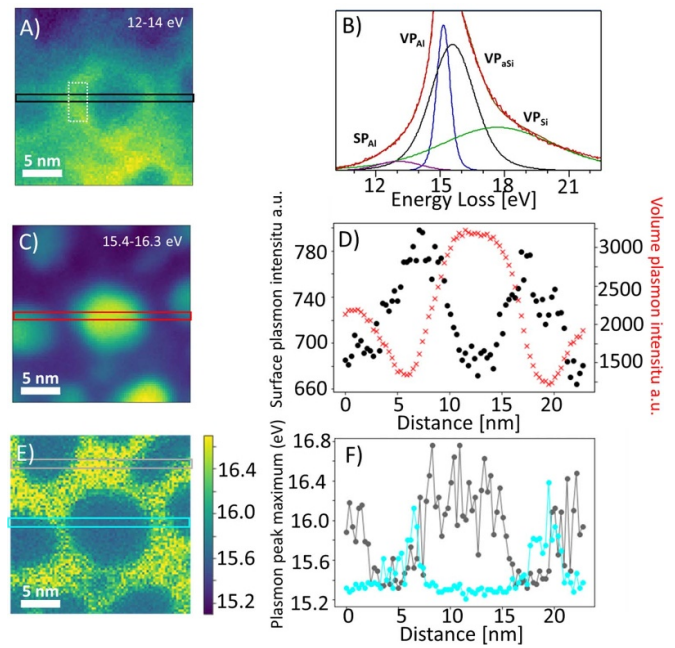


Figure 3. Al nanowire in plane-view. (A) Mapping the plasmon peak at 12–14 eV, (B) EELS low loss peak of the AlNW/*a*–*Si* interface (area shown in (A)) fitted with Gaussian–Lorentzian components, (C) plasmon mapping of 15.4–16.3 eV, (D) Graph of the plasmon intensities across the NW in figure, (A) and (C) (area shown in (C)) across the AlNW, (E) mapping of the plasmon peak maximum, (F) line-profile of plasmon peak maxima across AlNWs in two areas shown in E.

the dipole longitudinal mode at 2.1 eV. The peak energies of the dipole modes obtained from the two different simulation methods is the same, indicating their credibility. By comparing figure 2(B) (light excitations) and C (electron beam source), we can observe that the transverse modes appear to be more intense than the longitudinal modes for an electron beam source, especially in the plane-view.

3.2. AlNWs in plane-view

3.2.1. Experimental (plane-view). First, we present the results from the AlNWs in the plane-view. From the EEL spectra of the interface between the AlNW and *a*–*Si*, a peak between 12–14 eV was observed. This peak is spatially resolved in figure 3(A) which shows a map of the integrated EEL signal between 12–14 eV in the location of an AlNW in plane-view. Figure 3(B) shows an EEL spectrum of the *a*–*Si*/AlNW-interface from the location of the white rectangle in figure 3(A). The spectrum was fitted with Gaussian–Lorentzian (GL) components and presented a peak at approximately 13 eV. The integrated signal between 15.4 eV and 16.3 eV, which corresponds to the location of the VP peak of Al, has been mapped in figure 3(C). To combine these findings, the intensity profiles of each pixel in figure 3(A) (black area) and figure 3(C) (red area) across the AlNW are plotted in figure 3(D). The SP peak shown in both figure 3(A) and B is located at the edges of the NW (black curve in figure 3(D)), while the VP is on the NW (red curve).

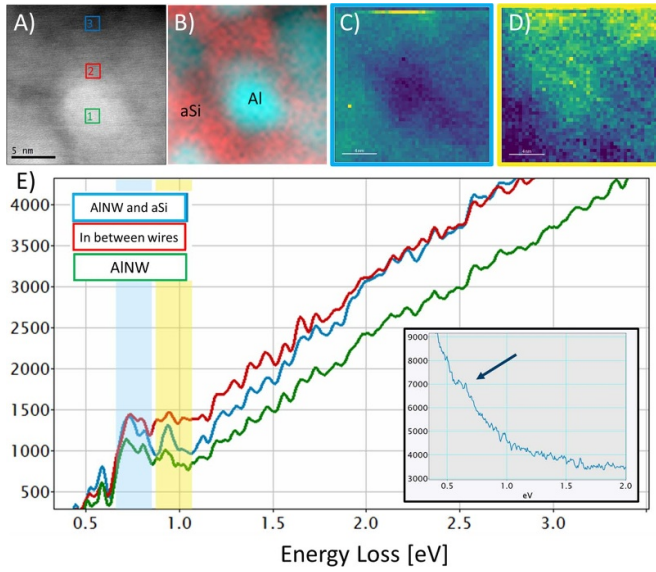


Figure 4. (A) HAADF STEM image of AlNW in *a-Si* in plane-view. (B) Energy filtered image using the bulk plasmon peak of *a-Si* (17.4 eV (red)) and Al (16 eV (blue)). (C) Energy filtered image of 0.7–0.9 eV of the low loss spectrum, (D) energy filtered image of 0.9–1.1 eV, and (E) the low loss spectrum of the selected regions in A with an inset of the unprocessed low loss EELS spectrum of region 2.

The properties of the *a-Si* surrounding the AlNWs were explored by analyzing the volume plasmons (VP). In figure 3(E) the energy loss position of the VP peak (red curve in figure 3(B)) is mapped, that is, the color refers to the VP peak energy at that point in the image. The VP maximum variations across (cyan area) and between (gray area) the AlNWs are plotted in figure 3(F). The VP peak maximum in the center of the AlNW was found to be approximately 15.2 eV, whereas the VP peak maximum between the wires (where we have *a-Si*) was found to vary between 15.5–16 eV. The *a-Si* near the *a-Si*/AlNW has a VP maximum of 16 eV, while the *a-Si* further away from the boundary of the AlNW has a peak at 15.5 eV. In contrast, there were no observable variations in the maximum VP_{Al} across the AlNW. The variation in the VP_{a-Si} energy is probably due to a change in the Al doping concentration. A spatially varying VP energy most probably implies the same for the dielectric response of the matrix which further can influence the SP response.

To investigate SPs with higher energy resolution, low loss EELS spectra (with lower dispersion) and energy mapping of the AlNWs in plane-view are shown in figure 4. Figure 4(A) presents a high-angle annular dark field (HAADF) STEM plane-view image of an AlNW in *a-Si*. Figure 4(B) shows an energy filtered image using the bulk plasmon peak of *a-Si* (16.8 eV (red)) and Al (15.2 eV (blue)). This image shows the location of both pure Si and Al in the selected area. The low loss EELS spectra of the three regions marked in figure 4(A) are shown in figure 4(E) with an inset of the unprocessed spectrum from area 2 (in between wires). There are two small intensity peaks just below the band gap of *a-Si* (which should be around 1.4 eV) at 0.75 eV and 0.9 eV. As shown by the unprocessed spectrum in the inset, the peak at 0.75 eV is

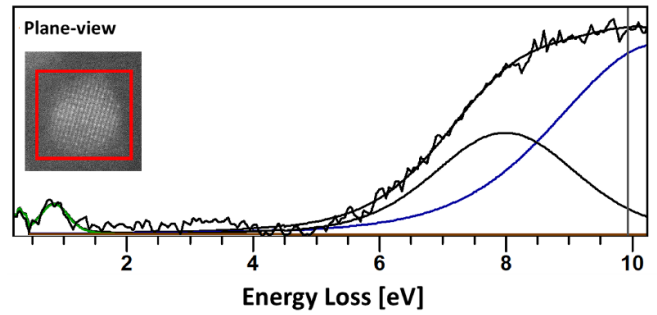


Figure 5. EELS low-loss spectra of Al nanowire in plane-view after subtracting a low loss spectrum of *a-Si*.

visible before background subtraction. Figure 4(C) shows an image of the integrated signal in the blue region of (E) (0.6–0.8 eV), while figure 4(D) shows an image of the integrated signal of the yellow region (0.9–1.1 eV). From the images, the signal from the blue region (at 0.75 eV) appears to be mainly from the *a-Si* between the AlNWs, while the signal from the yellow region (at 0.9 eV) may be from the AlNWs.

We were able to more closely analyze the plasmon peaks resulting from the AlNWs in a low dispersion low loss EEL spectrum by subtracting a pure *a-Si* signal from the AlNW spectrum (after normalizing to the onset of the spectrum) as shown in figure 4. The subtracted *a-Si* spectrum was obtained from a clean *a-Si* area with no visible AlNWs, in cross-sectional view (spectra shown in figure S3). The results from these AlNWs in the plane-view are shown in figure 5. The AlNW has plasmon peaks at 0.9 eV, 7.9 eV and 10.5 eV. The peak at 0.75 eV is not visible. However, this region was used to normalize the spectra before subtraction, which could have influenced the peaks in the region. The peak at 10.5 eV is at an energy similar to that of the dipole transverse peak in the simulated results of an AlNW in vacuum (see figure 2). The agreement between the experiments and simulations implies that there was no significant shift from embedding the NW in the *a-Si* matrix. We will investigate this point further later in this study.

3.2.2. Calculations (plane-view). Furthermore, simulated EELS maps of the wires were created to visualize the SP modes represented by the peaks in the simulated \bar{P}_{loss} spectra in figure 2 and compared with the experimental data shown in figure 3. The electron energy loss probability is given by [31]

$$P_{\text{loss}} = -\frac{q}{\pi\hbar\omega} \int dt \Re\{e^{i\omega t} \vec{v} \cdot \vec{E}^{\text{ind}}[\vec{x}(t), \omega]\}. \quad (1)$$

Here q is the electron charge, where ω is the frequency, \vec{v} is the electron velocity, $\vec{x}(t)$ is the straight-line trajectory of the electron and \vec{E}^{ind} is the induced electric field from the SP mode. This equation shows that P_{loss} is not directly proportional to the total electric field strength of the induced SP mode, but to the part of \vec{E}^{ind} that is parallel to \vec{v} . Figure 6(A) shows the loss probability distribution at the peak energy of the three lowest energy peaks (at 2.1 eV, 3.7 eV and 4.9 eV), where 2.1 eV is the dipole longitudinal mode (see figure 2). Additionally,

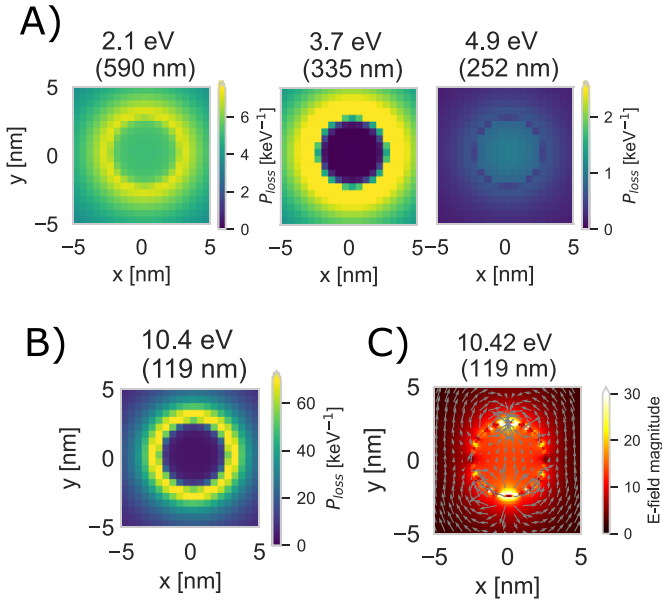


Figure 6. (A) Simulated EELS maps of the three most dominant longitudinal modes at low energy shown in plane-view. (B) Simulated EELS maps of the dipole transverse mode. (C) Electric field magnitude and arrows showing the direction of the field of the dipole transverse mode excited by a plane wave in the x - y plane, i.e. a cross section in the middle of the wire. The electric field of the plane wave is directed in the y -direction.

figure 6(B) shows the loss probability distribution at the dipole transverse peak (at 10.4 eV) that appeared in both the light excited and electron excited simulations (figure 2(B) and (C), respectively). The maps at energies representing the SP peaks at 2.1 eV, 3.7 eV and above 9.3 eV (see figure S7) have more loss at the mantle of the wire compared to inside, while the rest of the SP modes between 3.7 eV and 9.3 eV have more loss inside the wire. From equation (1), a low loss probability can imply either a low electric field or that the induced electric field is perpendicular to the electron velocity. Figure S8 shows that the electric field inside the wire in the dipole longitudinal mode at 2.1 eV is parallel to the electron velocity in plane view but very weak compared to that outside the wire. In the higher order longitudinal modes, from 4.9 eV and above, (see figure S7), the electric field strengths are more similar outside and inside the wire which could explain the maps in figure 6(A). Figure 6(C) shows the electric field in a cross section of the wire. The map shows that the electric field is largest at the location where we expect there to be largest charge density because the electric field is in the y -direction. The simulated EELS map show a similar result when one considers that the electron can excite the dipole mode in any direction in the x - y -plane in contrast to the plane wave excitation. Looking at figure 3(A) in light of these calculations, it seems most likely that the SP at 13 eV is a transverse type SP, since it is at much higher energy than 3.7 eV and has most loss at the mantle compared to inside the wire.

Experimentally, the nanowires are not isolated, but are located near other nanowires. Therefore, the interactions between the SP modes of two nearby NWs were investigated. Figure 7

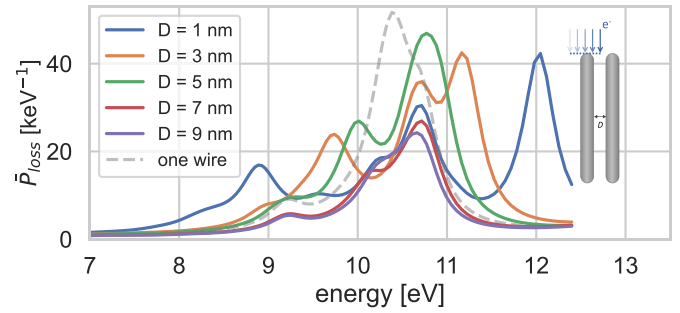


Figure 7. (A) Absorption cross sections with increasing distance between the wires, D , shown for a plane wave in two different directions.

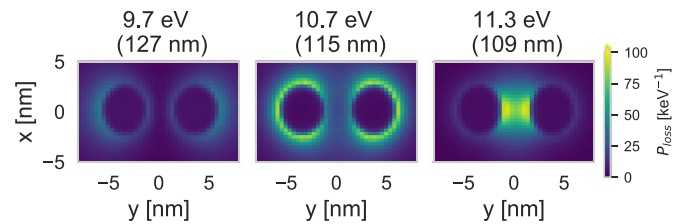


Figure 8. Loss probability maps of two wires separated by 3 nm distance, at the peak energies shown in figure 7 in plane-view, at 9.7 eV, 10.7 eV, and 11.3 eV.

shows the simulation results of the loss probability of two wires in plane-view with varying distance, D . An illustration of the electron beam scanning path is provided in the inset of the plot. The resulting \bar{P}_{loss} spectra show the transverse mode separate into three distinct peaks when $D \leq 3$ nm. The electron source can excite both red-shifted and blue-shifted interacting modes simultaneously compared to light where it is dependent on the polarization. The separate red-shifted and blue-shifted interacting modes and their polarization dependence are elaborated on in the SI and shown in figure S9. One can observe that the peaks in the simulated EELS spectra are very similar to the peaks from the light excitation. That implies that these are bright modes. The experimental nanowires were separated by 1.5–2.5 nm. Thus, from these simulation results one expected the transverse peak to split into different peaks around 10.4 eV due to interactions.

Figure 8 shows simulated EELS maps in plane-view. The maps were made at the peak energies of the two AlNWs separated by 3 nm distance, resembling the experimental sample shown in figure 4. The leftmost map at 9.7 eV shows that for the red-shifted peak energy the electron energy loss is localized on the part of the mantle that points away from the other AlNW. This mode is probably a bonding mode, while the blue-shifted peak at 11.3 eV (to the right) is an anti-bonding mode. The anti-bonding mode has anti-symmetric electric fields which results in fields pointing away from the region between the wires [18]. The field results in greatest loss between the wires. In the bonding mode, contrary to the P_{loss} distribution, the electric field is high between the wires because it has symmetric fields pointing from one dipole to the other between the wires. However, the field is perpendicular

to the electron velocity which results in a low loss probability. The map at 10.7 eV probably show a peak representing interactions between the dipole mode and higher-order modes [32]. The different interacting modes, and their polarization dependence, are elaborated on in SI and figure S10. In figure 3, we show a SP peak at approximately 13 eV with high intensity on the mantles of the wires as well as between them. The maps discussed above hence indicate that the experimental maps resemble both bonding and anti-bonding modes.

We performed simulations at energies below 3 eV for comparison with our experimental data, as shown in figure 4. In these simulations, a different dielectric function source (McPeak *et al* [33]) was used for Al. It has more data points at low energies compared to the source used in the other simulations (Rakic [34]). The dipole longitudinal mode has a slightly different energy with the new dielectric function source. This is discussed in SI and figure S11. The spectra of an AlNW in a core-shell configuration with an $a-Si$ shell of different thickness, t , is shown. A core-shell configuration was used as an approximation of an AlNW embedded in $a-Si$. The lowest-energy mode in the spectra is most likely the dipole longitudinal mode, based on the map of the modes in the cross-sectional view in figure S12(B). By comparing the peak energies with the energy of the dipole longitudinal peak with no shell, we observe a red-shift of at least 0.5 eV, by the surrounding $a-Si$. We therefore suggest that the peak at 0.75 eV in figure 4 is the dipole longitudinal peak. This is because both the experimental results and simulated maps in figure 9(B) show that these modes have more loss in the surrounding $a-Si$ than in the AlNW itself. The peak at 1.5 eV is probably the interband peak and has accordingly most loss in the AlNW. However, a peak with the same behavior as the 0.9 eV peak was not found at energies below 1 eV in the simulations.

3.3. AlNWs in cross-sectional view

3.3.1. Experimental (cross-sectional view). The EELS results of the SP and VP of the AlNWs in cross-sectional view are shown in figure 10. The map of the integrated signal between 12 and 14 eV (corresponding to the energy of the SP peak observed in figures 3(A) and (D)) is shown in figure 10(A), while the integrated signal between 15.4–16.3 eV (corresponding to the energy of the VP_{Al}) is mapped in figure 10(B). The average signal in the y -direction at a certain position, x , is shown in figure 10(C). The colors correspond to the areas marked with rectangles in A (black) and B (red). The intensity profile in the 12–14 eV region shows a small increase in intensity on the surface of the AlNWs, therefore again indicating that this is signal from a transverse SP mode.

In order to investigate the optical regime, low loss EELS with higher energy resolution was performed. Figure 11 shows five images with the integrated signal regions of 2.6–4.3 eV, 4.5–5.5 eV, 6.0–7.0 eV, 7.3–7.9 eV, and 9.3–10.3 eV, of an AlNW in cross-sectional view. EELS low loss spectra from one of the AlNWs (red area) and the area between the AlNWs (black area) are shown, with fitted Gaussian-Lorentzian peaks. The location of the extracted spectra is shown in the first energy filtered image (2.6–4.3 eV). The images show that the

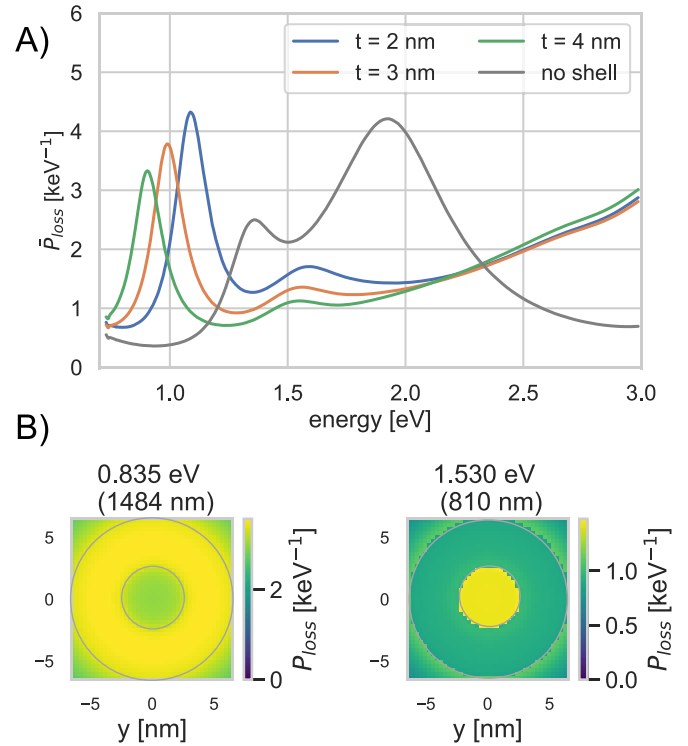


Figure 9. (A) Simulated EELS spectra in plane-view (see figure 2(A) of a AlNW with same size as before, but with a $a-Si$ shell at different thickness, t . Included for comparison is the spectrum from a AlNW in vacuum with no shell. (B) Simulated EELS map showing the loss probability distribution in plane-view at the energy of the two largest peaks in the spectrum for $t = 4$ nm. The AlNW- $a-Si$ boundary and the $a-Si$ -vacuum boundary are marked with grey circles.

AlNW have peaks at 2.5 eV, 5 eV, 7.9 eV, and 10.5 eV, while the ‘in-between NWs’-spectrum from aSi shows peaks at 2 eV, 3 eV, 4.6 eV, 6.6 eV, and 10.5 eV. Mapping the energy loss region at 7.3–7.9 eV shows that this signal can mainly be found at the side-walls of the AlNW and on the $c-Si/a-Si$ interphase, while the peak at 10.5 eV also shows loss at the side-walls but has more loss around the whole wire and towards the vacuum and less loss towards the interphase. The thickness of the sample in this area is approximately 20 nm and it is wedge-formed. Hence, some of the wires might be exposed to vacuum, while others surrounded by $a-Si$ or SiO_x (near the surface of the wedge). The results may therefore not be exactly the same as those in a bulk sample where all the wires are embedded in $a-Si$. Variations in the environment influence the SPs. It is difficult to quantify this varying environment from TEM measurements, which makes it difficult to simulate the exact same system and understand all the different SP modes from the experimental data. Notwithstanding, the use of TEM and EELS in this manner results in valuable information which is not possible to obtain using other techniques.

The EELS spectrum of an AlNW after subtracting the $a-Si$ signal is shown in figure 12. The AlNW is found to have a plasmon at 4.4 eV, 7.9 eV and 10.5 eV in the cross-sectional view, the latter two are very similar to the two found in the

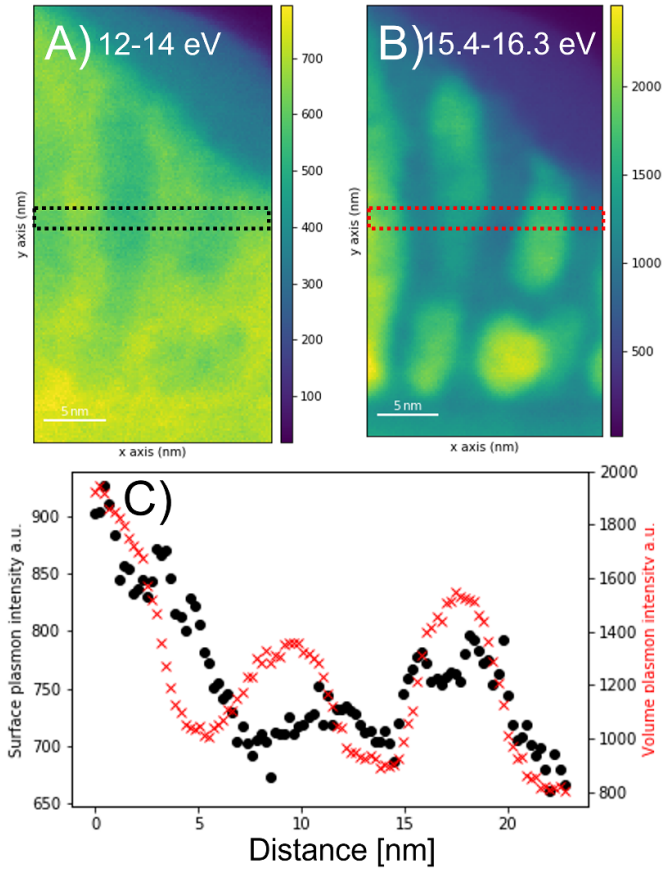


Figure 10. Al nanowire in cross-sectional view. (A) Mapping the plasmon peak at 12–14 eV, (B) plasmon at 15.4–16.3 eV, and (C) graph of the plasmon intensities from image A and B (stippled square) across the AlNWs.

plane-view with the same method (see figure 5). The additional peak could be a mode that is more easily excited in the cross-sectional view owing to the direction of the electron beam compared to \vec{E}_{ind} . An example from the simulations is the longitudinal mode at 4.9 eV which is only visible in the spectrum from the cross-sectional view (see figures 2(C) and S16).

3.3.2. Calculations (cross-sectional view). We have additionally simulated the AlNWs in cross-sectional view in order to compare with the experimental results of the plasmonic modes. Figures 13(A) shows the loss probability distribution at the peak energy of the three lowest energy peaks in cross-sectional view (at 2.1 eV, 3.7 eV, and 4.9 eV), where 2.1 eV was the dipole longitudinal mode. The cross-sectional view shows that the dipole longitudinal mode had the largest P_{loss} , at the tip of the nanowire. The other maps in figure 13(A) show that, with increasing energy, the number of nodes and antinodes along the wire increases. This is even more clear in figure S13 (in the SI) which shows all the SP modes excited by an electron from 2.1 eV to 9.3 eV in cross-sectional view. This correlates well with the calculated electric field in figure S8, which shows the corresponding optically excitable modes.

Figure 13(B) shows the loss probability distribution at the transverse mode (10.4 eV) and figure 13(C) shows the electric

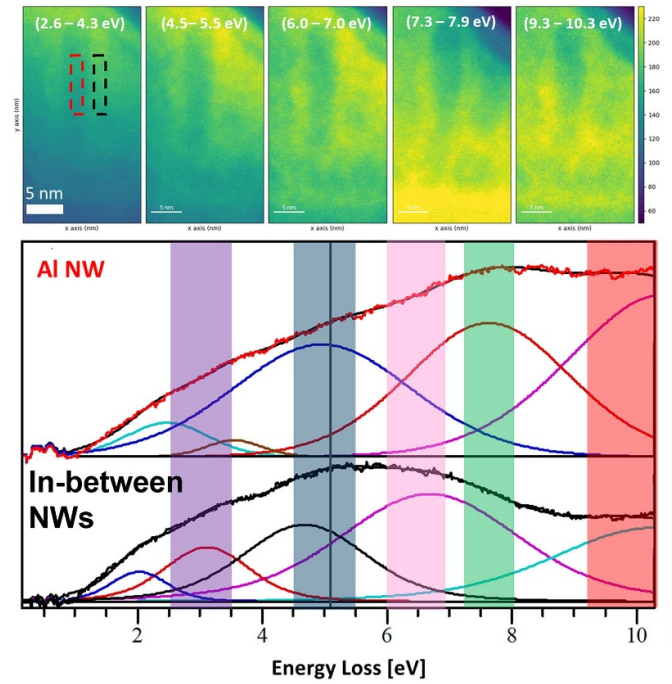


Figure 11. Energy filtered images of the sample in cross-sectional view, showing five energy loss intervals with two EELS low loss spectra, from the AlNW and in-between AlNWs.

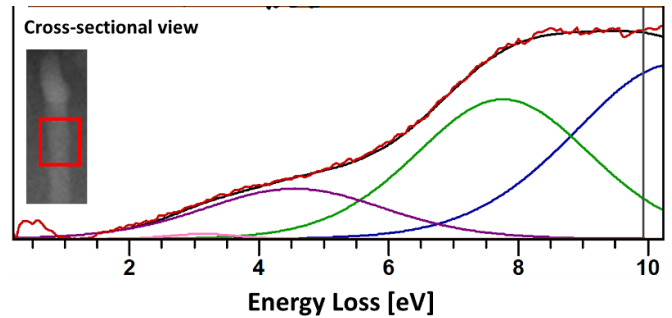


Figure 12. EELS low-loss spectra of Al nanowire in cross-sectional view after subtracting a low loss spectrum of *a*-Si.

field in a cross section of the wire when the incoming electric field is parallel to the *y*-axis. The electric field is higher at the mantle of the wire compared to inside the wire. A higher loss is also observable at the wire mantle in the P_{loss} distribution shown in figure 13(B). The loss probability is surprisingly similar to the electric field magnitude considering that the direction of the induced electric field is important in the loss probability and that the electron can excite the transverse mode in other directions than in the *y*-direction. The loss distribution is similar, however, to experimental SP maps of the transverse mode in a Ag rod [35].

Similar to the plane-view, we investigated the interaction of the modes in the cross-sectional view, as shown in figure 14. The maps were made at the peak energies of the two AlNWs separated by a distance of 3 nm, i.e. a little more than the distance in the experimental sample shown in figure 11. The leftmost map (at 9.7 eV) shows that for the red-shifted peak

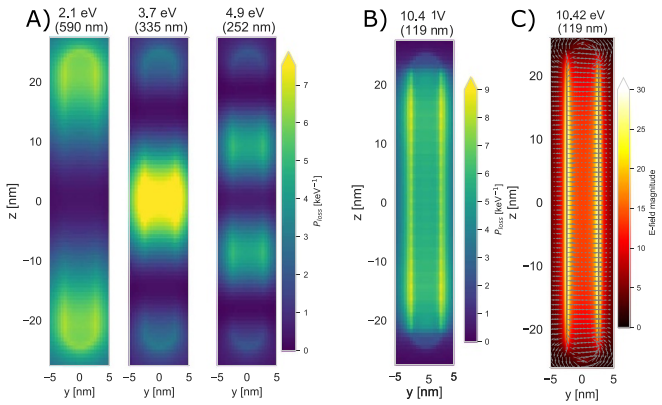


Figure 13. (A) Simulated EELS maps of the three most dominant longitudinal modes at low energy shown in cross-sectional view. (B) Simulated EELS maps of the dipole transverse mode. (C) The electric field magnitude and field lines of the dipole transverse mode in the y - z -plane. The transverse mode is excited by a plane wave with an electric field in the y -direction.

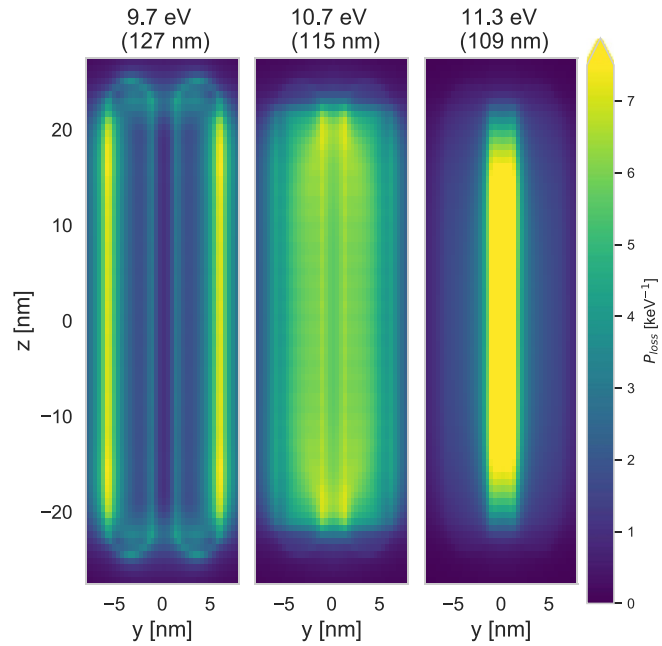


Figure 14. Loss probability maps of two wires separated by 3 nm distance, at the peak energies shown in figure 7 in cross section.

energy, most of the loss occurs on the part of the mantle that points away from the other AlNWs (bonding mode), as shown in the plane-view images in figure 8. The blue-shifted peak at 11.3 eV is an anti-bonding mode, as in the case of the plane view. The map at 10.7 eV resembles the transverse dipole mode in a single wire, as shown in figure 13 except that in the interacting case, the loss probability is higher on the side of the mantle pointing towards the other AlNW. This is opposite to that observed in the plane-view in figure 8. This could be due to the electron beam direction being different in plane-view and cross-sectional view compared with the direction of the induced electric field.

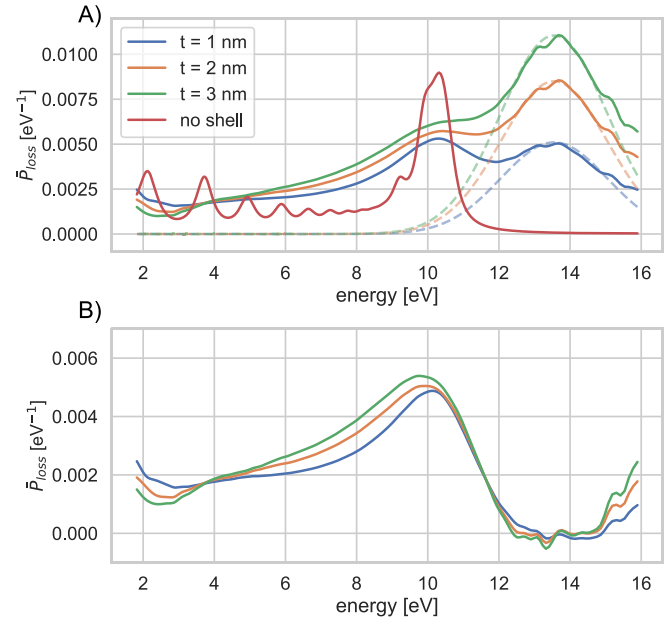


Figure 15. (A) Simulated EELS spectra in cross-sectional view (see figure 2(A) of a AlNW with same size as before, but with a thin $a - Si$ shell at different thickness, t . Included for comparison is the spectrum from a AlNW in vacuum with no shell. A Gaussian fit to the bulk plasmon of $a - Si$ is also shown in dashed lines. (B) Spectra from (A) with the Gaussian fit subtracted.

In the experimental data in figure 11, we see that some of the peaks only appear in the ‘in-between NWs’ spectrum (i.e. 3 eV, 4.6 eV and 6.6 eV). From the simulation of interacting wires, it looks as if these peaks originate from anti-bonding interacting modes, which in the case of the transverse mode have more loss between the two wires and very little loss in the AlNW. A similar behavior was observed for the anti-bonding longitudinal modes in figure S14(C). On the other hand, the modes that are strongest in the AlNW-spectrum (i.e. 5 eV, 7.9 eV and 10.5 eV) resemble the 10.7 eV mode in figure 14 where there is lower contrast between the loss from the wire itself than between the wires.

To determine how the peak at approximately 10.5 eV is influenced by the wire being surrounded by $a - Si$ instead of vacuum, we employed the same core-shell configuration as described for plane-view, but this time in cross-sectional view. As shown in figure S15, the real part of the refractive index of $a - Si$, n , is small at 10 eV, that is, approximately 0.5 while the imaginary part, κ , is approximately 1. Therefore, we cannot assume that the peak is red-shifted as in the case below 3 eV where n is approximately 4. Figure 15(A) shows \bar{P}_{loss} of the core-shell particle with different shell thicknesses (t). The bulk plasmon of $a - Si$ is also observed at 13 eV, which is very low compared to the experimental data and discredit the dielectric function of the $a - Si$ used here. However, the data was stated to be experimental up to 12 eV, so we assumed that it is a good representation of the dielectric function up to that point. The simulated spectrum from the wire without a shell (red spectrum) is also shown. A shoulder at the same energy as the transverse peaks (approximately 10.4 eV in the red spectrum) is clearly visible in the spectra of the core-shell particles.

The figure also shows a Gaussian fit to VP_{a-Si} . Figure 15(B) shows the same spectra as in figure 15(A), except that the Gaussian fit to VP_{a-Si} was subtracted. The subtraction shows that the peak around 10 eV is slightly red-shifted with increasing thickness of the $a-Si$ shell, but there is no large red-shift when we compare the peak in vacuum with the peak in a core-shell (Al- $a-Si$) particle.

4. Summary and conclusion

In this study we measured and modelled the LSPR and VP properties of self-organizing AlNWs with diameters of approximately 3–5 nm, embedded in an $a-Si$ matrix. A combination of experimental results with modelled structures is crucial for understanding how the plasmonic properties behave at the nanoscale, and how they can be tuned for certain applications.

We found several SP modes experimentally in the plane-view (0.75 eV, 0.9 eV, 7.9 eV, 10.5 eV and 13 eV) and cross-sectional view (4.4 eV, 7.9 eV, 10.5). All modes from the experiments and modelling are summarized in figure S16 in the SI. The peak at 13 eV is most likely a transverse mode, but a peak at the same energy was not observed with the modelling. This also applies to the mode at 7.9 eV. We observed a peak in the experimental data, but not by modelling. However, we have observed that the plasmon peak at 10.7 eV can split into red-shifted and blue-shifted peaks when two wires are placed close together. Our modelling results show that with a wire separation of 1 nm, the red-shifted peak is at 8.9 eV and the blue-shifted at 12.1 eV. In order to shift these two peaks further, to 7.9 eV and 13 eV as seen from our experiments, there may be other factors to consider such as the presence of $a-Si$ in-between the wires.

The peak at 10.5 eV was found both experimentally and by modelling. We showed that surrounding the wire with $a-Si$ does not change the peak energy within this energy range; hence, we presume that this is the dipole transverse peak. Furthermore, the peak at 4.4 eV found experimentally in the cross-sectional mode was not found by modelling. However, the experimental nanowires were around 20 nm long. The dipole longitudinal mode of a 20 nm AlNW in vacuum is at around 4 eV (see figure S4), but in this energy range the refractive index of aSi is high and can red-shift peaks significantly. Therefore, the peak found in the experiments is probably not the dipole longitudinal mode. It could be a higher order longitudinal peak, but these seem to have a lower intensity compared to the dipole mode. Thus making it odd that we do not observe another peak at lower energies. Further down in energy, in plane-view, we have two peaks just below 1 eV in the experimental data, at 0.75 eV and 0.9 eV. In the case of modelling, we showed that the high refractive index of $a-Si$ in this energy range, red-shifts the dipole longitudinal peak of a 50 nm long AlNW below 1 eV from its original energy of approximately 2 eV in a vacuum. In addition, the dipole longitudinal peak can be red-shifted by increasing the length (figure S4). Therefore, we believe that one of these plasmon peaks was the dipole longitudinal peak.

Our simulated results show that the size, distance between wires, and embedding material have a significant impact on the SP energy that will be available in the material. Tuning these properties for appropriate applications is important. Plasmonic properties of a material for sensing capabilities, require a distinct and sharp LSPR peak that moves easily when in contact with gas molecules [36]. On the other hand, for catalytic applications, the material should both preferentially absorb light and act as a catalytic surface. For these materials, the plasmon oscillations decay into hot-electrons that can weaken chemical bonds and accelerate the catalytic reaction [37]. This does not require a single LSPR peak but can have many over a set range. For our sample with an AlNW size of 3–5 nm and NW separation of 1.5–2.5 nm, the peaks are blue- and red-shifted, and more peaks interact. This results in many smaller plasmon peaks that are more suitable for catalysis. Samples with a greater distance between the wires could enable sensing technologies as the preferential application domain.

We have investigated the plasmonic properties of AlNWs in $a-Si$ using EELS and FDTD modelling. LSPRs from 0.9 eV to 10.7 eV have been observed, which include the UV and VUV range. Therefore, these LSPRs can be used to enhance high energy photocatalytic reactions in this energy range.

Data availability statement

The data that support the findings of this study are available upon reasonable request from the authors.

Acknowledgment

This work is part of the Projects ‘Nanosol’ (Grant No. 231658) and ‘FUNCTION’ (Grant No. 287729), financially supported by the Research Council of Norway. SuperSTEM is the National Research Facility for Advanced Electron Microscopy funded by the Engineering and Physical Sciences Research Council (EP/W021080/1). The Research Council of Norway is also acknowledged for its support from The Norwegian Transmission Electron Microscopy Centre (197405).

ORCID iDs

Annett Thøgersen  <https://orcid.org/0000-0002-4064-1887>

Branson D Belle  <https://orcid.org/0000-0002-1211-8714>

Vilde Mari Reinertsen  <https://orcid.org/0000-0002-8946-2812>

Øystein Prytz  <https://orcid.org/0000-0001-6679-6492>

Demie Kepaptsoglou  <https://orcid.org/0000-0003-0499-0470>

References

- [1] Atwater H and Polman A 2010 *Nat. Mater.* **9** 205
- [2] Sheldon M T, van de Groep J, Brown A M, Polman A and Atwater H A 2014 *Science* **346** 828
- [3] Tam F, Goodrich G, Johnson B and Halas N J 2007 *Nano Lett.* **7** 496

- [4] Martin J, Kociak M, Mahfoud Z, Proust J, Gerard D and Plain J 2014 *Nano Lett.* **14** 5517
- [5] Linic S, Aslam U, Boerigter C and Morabito M 2015 *Nat. Mater.* **14** 567
- [6] Bergman D J and Stockman M I 2003 *Phys. Rev. Lett.* **90** 027402
- [7] Barnes W L, Dereux A and Ebbesen T W 2003 *Nature* **424** 824
- [8] Knight M W, Liu L, Wang Y, Brown L, Mukherjee S, King N S, Everitt H O, Nordlander P and Halas N J 2012 *Nano Lett.* **12** 6000
- [9] Hobbs R G, Yang Y, Fallahi A, Keathley P D, De Leo E, Kärtner F X, Graves W S and Berggren K K 2014 *ACS Nano* **8** 11474
- [10] Hobbs R G, Manfrinato V R, Yang Y, Goodman S A, Zhang L, Stach E A and Berggren K K 2016 *Nano Lett.* **16** 4149
- [11] Wolf M, Nettesheim S, White J M, Hasselbrink E and Ertl G 1991 *J. Chem. Phys.* **94** 4609
- [12] Langhammer C, Schwind M, Kasemo B and Zorić I 2008 *Nano Lett.* **8** 1461
- [13] Gérard D and Gray S K 2014 *J. Phys. D: Appl. Phys.* **48** 184001
- [14] Knight M, King N, Liu L, Everitt H, Nordlander P and Halas N J 2014 *ACS Nano* **8** 834
- [15] Schaffer B, Grogger W, Kothleitner G and Hofer F 2010 *Ultramicroscopy* **110** 1087
- [16] Asselin J, Boukouvala C, Hopper E R, Ramasse Q M, Biggins J S and Ringe E 2020 *ACS Nano* **14** 5968
- [17] Bosman M, Keast V J, Watanabe M, Maarroof A I and Cortie M B 2007 *Nanotechnology* **18** 165505
- [18] Colliex C, Kociak M and Stéphan O 2016 *Ultramicroscopy* **162** A1
- [19] Nelayah J 2007 *Nat. Phys.* **3** 348
- [20] Ringe E 2020 *J. Phys. Chem. C* **124** 15665
- [21] Egerton R F 2008 *Rep. Prog. Phys.* **72** 016502
- [22] Li G, Cherqui C, Bigelow N W, Duscher G, Straney P J, Millstone J E, Masiello D J and Camden J P 2015 *Nano Lett.* **15** 3465
- [23] Diaz-Egea C et al 2015 *Nanotechnology* **26** 405702
- [24] Sakaguchi N, Matsumoto S, Kunisada Y and Ueda M 2019 *J. Phys. Chem. C* **123** 6735
- [25] Thøgersen A, Jensen I J T, Stange M, Kjeldstad T, Martinez-Martinez D, Løvvik O M, Ulyashin A G and Diplas S 2018 *Nanotechnology* **29** 315602
- [26] Kjeldstad T, Thøgersen A, Stange M, Azarov A, Monakhov E and Galeckas A 2019 *Nanotechnology* **30** 135601
- [27] Kjeldstad T, Thøgersen A, Stange M, Jensen I T, Monakhov E and Galeckas A 2019 *Nanomaterials* **9** 1106
- [28] Kjeldstad T, Thøgersen A, Stange M, Jensen I, Nilsen O, Galeckas A and Monakhov E 2020 *Thin Solid Films* **702** 137982
- [29] I. ANSYS *Ansyz Lumerical FDTD Simulation of Photonic Components* (available at: <https://.ansys.com/products/photonics/fdtd>)
- [30] Hohenester U and Trügler A 2012 *Comput. Phys. Commun.* **183** 370
- [31] García de Abajo F J 2010 *Rev. Mod. Phys.* **82** 209
- [32] Nordlander P, Oubre C, Prodan E, Li K and Stockman M I 2004 *Nano Lett.* **4** 899
- [33] McPeak K M, Jayanti S V, Kress S J, Meyer S, Iotti S, Rossinelli A and Norris D J 2015 *ACS Photonics* **2** 326
- [34] Rakić A D 1995 *Appl. Opt.* **34** 4755
- [35] Rossouw D, Couillard M, Vickery J, Kumacheva E and Botton G A 2011 *Nano Lett.* **11** 1499
- [36] Duan Q, Liu Y, Chang S, Chen H and Chen J-H 2021 *Sensors* **21** 5262
- [37] Sun Y and Tang Z 2020 *MRS Bull.* **45** 20